Journal of Advanced Research 35 (2022) 231–243

Contents lists available at ScienceDirect

Journal of Advanced Research

journal homepage: www.elsevier.com/locate/jare

Nano-Honokiol ameliorates the cognitive deficits in TgCRND8 mice of Alzheimer's disease via inhibiting neuropathology and modulating gut microbiota

Chang Qu [a], Qiao-Ping Li [b], Zi-Ren Su [b], Siu-Po Ip [a,c], Qiu-Ju Yuan [a,c], You-Liang Xie [b], Qing-Qing Xu [a], Wen Yang [a], Yan-Feng Huang [a], Yan-Fang Xian [a,c,*], Zhi-Xiu Lin [a,c,d,*]

[a] School of Chinese Medicine, Faculty of Medicine, The Chinese University of Hong Kong, Hong Kong Special Administrative Region
[b] Guangdong Provincial Key Laboratory of New Drug Development and Research of Chinese Medicine, Mathematical Engineering Academy of Chinese Medicine, Guangzhou University of Chinese Medicine, Guangzhou 510006, China
[c] Brain Research Centre, School of Chinese Medicine, Faculty of Medicine, The Chinese University of Hong Kong, Hong Kong Special Administrative Region
[d] Hong Kong Institute of Integrative Medicine, The Chinese University of Hong Kong, Hong Kong Special Administrative Region

HIGHLIGHTS

- In the same content, Nano-HO could effectively enhance the bioactivity of HO remarkably and prolonged its circulation time in rats.
- Nano-HO improved cognitive deficits in TgCRND8 mice.
- Nano-HO suppressed neuroinflammatory response (TNF-α, IL-Iβ, IL-6) inhibited the activation of microglia, astrocyte and A-β plaque burdens in TgCRND8 mice.
- Nano-HO ameliorated AD through regulating APP processing, preventing tau hyperphosphorylation and modulating JNK/CDK5/GSK-3β pathway.
- Nano-HO regulated the composition and structure of gut microbiota to protect the gut microflora and its stability.

GRAPHICAL ABSTRACT

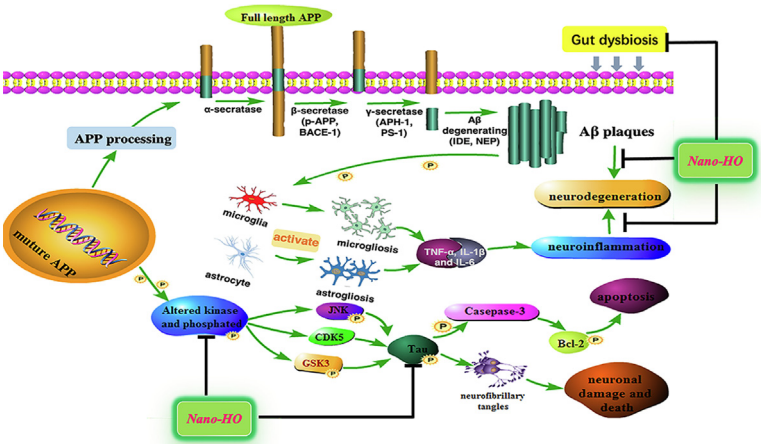

ARTICLE INFO

Article history:
Received 25 October 2020
Revised 8 March 2021
Accepted 28 March 2021
Available online 31 March 2021

ABSTRACT

Introduction: Honokiol (HO) exerts neuroprotective effects in several animal models of Alzheimer's disease (AD), but the poor dissolution hampers its bioavailability and therapeutic efficacy.
Objectives: A novel honokiol nanoscale drug delivery system (Nano-HO) with smaller size and excellent stability was developed in this study to improve the solubility and bioavailability of HO. The anti-AD effects of Nano-HO was determined.

Abbreviations: AD, Alzheimer's disease; Aβ, β-amyloid; APH-1, anterior pharynx-defective-1; APP, amyloid precursor protein; BACE-1, β-site APP cleaving enzyme-1; Bcl-2, B cell lymphoma-2; CDK5, cyclin-dependent kinase 5; CMC-Na, sodium carboxymethylcellulose; GSK-3β, glycogen synthase kinase 3β; HO, Honokiol; HPLC, high performance liquid chromatography; IDE, insulin degrading enzyme; IL-6, interleukin 6; IL-1β, interleukin 1β; PS-1, presenilin-1; JNK, c-Jun N-terminal kinase; MCT, Medium-chain triglycerides; MWMT, Morris Water Maze test; Nano-HO, honokiol nanoscale drug delivery system; NEP, neprilysin; NFTs, neurofibrillary tangles; PBS, phosphate-buffered saline; PDI, poly-dispersity index; ROS, reactive oxygen species; TEM, transmission electron microscope; TNF-α, tumor necrosis factor; WT, wild type; ZP, zeta potential.

Peer review under responsibility of Cairo University.

* Corresponding authors at: Room 101-J, 1/F, Li Wai Chun Building, The Chinese University of Hong Kong, Hong Kong Special Administrative Region.
E-mail addresses: lisaxian@cuhk.edu.hk (Y.-F. Xian), linzx@cuhk.edu.hk (Z.-X. Lin).

https://doi.org/10.1016/j.jare.2021.03.012
2090-1232/

Keywords:
Honokiol nanoscale drug delivery system
TgCRND8 mice
Cognitive deficits
Neuroinflammation
Tau protein hyperphosphorylation
Gut microbiota

Methods: Male TgCRND8 mice were daily orally administered Nano-HO or HO at the same dosage (20 mg/kg) for 17 consecutive weeks, followed by assessment of the spatial learning and memory functions using the Morris Water Maze test (MWMT).
Results: Our pharmacokinetic study indicated that the oral bioavailability was greatly improved by Nano-HO. In addition, Nano-HO significantly improved cognitive deficits and inhibited neuroinflammation via suppressing the levels of TNF-α, IL-6 and IL-1β in the brain, preventing the activation of microglia (IBA-1) and astrocyte (GFAP), and reducing β-amyloid (Aβ) deposition in the cortex and hippocampus of TgCRND8 mice. Moreover, Nano-HO was more effective than HO in modulating amyloid precursor protein (APP) processing via suppressing β-secretase, as well as enhancing Aβ-degrading enzymes like neprilysin (NEP). Furthermore, Nano-HO more markedly inhibited tau hyperphosphorylation via decreasing the ratio of p-Tau (Thr 205)/tau and regulating tau-related apoptosis proteins (caspase-3 and Bcl-2). In addition, Nano-HO more markedly attenuated the ratios of p-JNK/JNK and p-35/CDK5, while enhancing the ratio of p-GSK-3β (Ser9)/GSK-3β. Finally, Nano-HO prevented the gut microflora dysbiosis in TgCRND8 mice in a more potent manner than free HO.
Conclusion: Nano-HO was more potent than free HO in improving cognitive impairments in TgCRND8 mice via inhibiting Aβ deposition, tau hyperphosphorylation and neuroinflammation through suppressing the activation of JNK/CDK5/GSK-3β signaling pathway. Nano-HO also more potently modulated the gut microbiota community to protect its stability than free HO. These results suggest that Nano-HO has good potential for further development into therapeutic agent for AD treatment.

Introduction

Alzheimer's disease (AD) is a neurodegenerative disease clinically characterized by progressive and irreversible cognitive impairments. Although the etiology of AD remains vague, aggressive amyloid-β (Aβ) deposition, intraneuronal neurofibrillary tangles (NFTs) and chronic neuroinflammation are the classic hallmarks of AD pathology [1]. Aβ is a proteolytic product of transmembrane amyloid precursor protein (APP) by amyloidogenic cleavage, which is sequentially processed by β-secretases (e.g., p-APP (Thr 688), β-site APP cleaving enzyme-1 (BACE-1)), γ-secretases (e.g., anterior pharynx-defective-1 (APH-1), presenilin-1 (PS-1)) and Aβ-degrading enzymes (e.g., insulin degrading enzyme (IDE), neprilysin (NEP)) [2]. Accumulation of Aβ surrounded by dystrophic neurites attributes to the formation of senile plaques, which are responsible for the cognitive dysfunction of AD [3]. On the other hand, tau hyperphosphorylation in the NFTs is triggered by the imbalance of the kinase/phosphatase system, including c-Jun N-terminal kinase (JNK), glycogen synthase kinase 3β (GSK-3β) and cyclin-dependent kinase 5 (CDK5) [4]. Among them, GSK-3β participates in the process of Aβ production and Aβ-mediated neuronal death by increasing tau hyperphosphorylation, finally forming insoluble masses of NFTs in neurons [5]. Additionally, tau phosphorylation is affected by the interaction of Aβ and CDK5, which leads to the cleavage of adjacent protein p-35 [4]. The aggregation of Aβ plaques and tau tangles is followed by microglia and astrocytes recruitment surrounding the plaques and local inflammatory response, thus the occurrence of neurotoxicity.

Currently, available drugs for AD can only ameliorate modest symptoms. Therefore, effective disease-modifying treatments for AD clearly remain an unmet medical need. Honokiol (HO, $C_{18}H_{18}O_2$, the chemical structure is shown in Fig. 1A), is a major active compound isolated from the dried bark of *Magnoliae Officinalis* Rehd. et wils. Recent studies have indicated that HO possesses neuroprotective effects in several animal models [6–9]. Nevertheless, the poor dissolution severely hampers its bioavailability. To overcome the intrinsic chemical solubility barrier of HO, we applied nano-particle drug delivery system (Nano-DDS) to formulate HO (thereafter termed "Nano-HO"). Nano-DDS is an anhydrous homogenous liquid mix of surfactant(s), cosurfactant, oil and drugs, which form oil-in-water (O/W) microemulsion when exposed to aqueous media under gentle agitation or digestive motility in gastro-intestinal (GI) tract [10]. Tiny globule size of Nano-DDS (20–100 nm) provides a large interfacial surface area, thereby improving drug absorption and bioavailability by enhancing drug release and membrane permeation, as well as reducing pre-systemic metabolism [10].

TgCRND8 mice, a well-characterized APP transgenic mouse model of AD, show a close association among Aβ deposition, neuroinflammation, tau hyperphosphorylation and cognitive impairments [11–12]. Therefore, TgCRND8 mice are suitable for discovering anti-AD agents in preclinical study. The aims of this study are (1) to explore whether Nano-HO could enhance the solubility and bioavailability of HO; (2) to investigate the cognitive deficit-ameliorating effects of Nano-HO; and (3) to illustrate the molecular mechanisms underlying the effects of Nano-HO on Aβ deposition, tau hyperphosphorylation, Aβ plaque-associated neuroinflammation, JNK/CDK5/GSK-3β signaling pathway and gut microbiota in TgCRND8 transgenic mice.

Material and methods

Chemical and reagents

Honokiol (purity ≥ 98% by high performance liquid chromatography (HPLC) analysis) was provided by Prof. Zi-Ren Su of Guangzhou University of Chinese Medicine. Its identity was confirmed by comparing its ^{1}H NMR and ^{13}C NMR spectra with that published in the literature [13]. Donepezil hydrochloride (Cat No.: D6821; purity ≥ 98%) and PEG-400 were purchased from Sigma-Aldrich (St. Louis, MO, USA). Kolliphor® HS-15 (PEG-15-hydroxystearate) was obtained from BASF Chemical Company (Ludwigshafen, Germany). Medium-chain triglycerides (C8, MCT) was purchased from Guangdong Mingkang Flavors & Fragrances Co., Ltd. (Guangzhou, Guangdong, China). All other chemicals and reagents used in this study were of analytical grade.

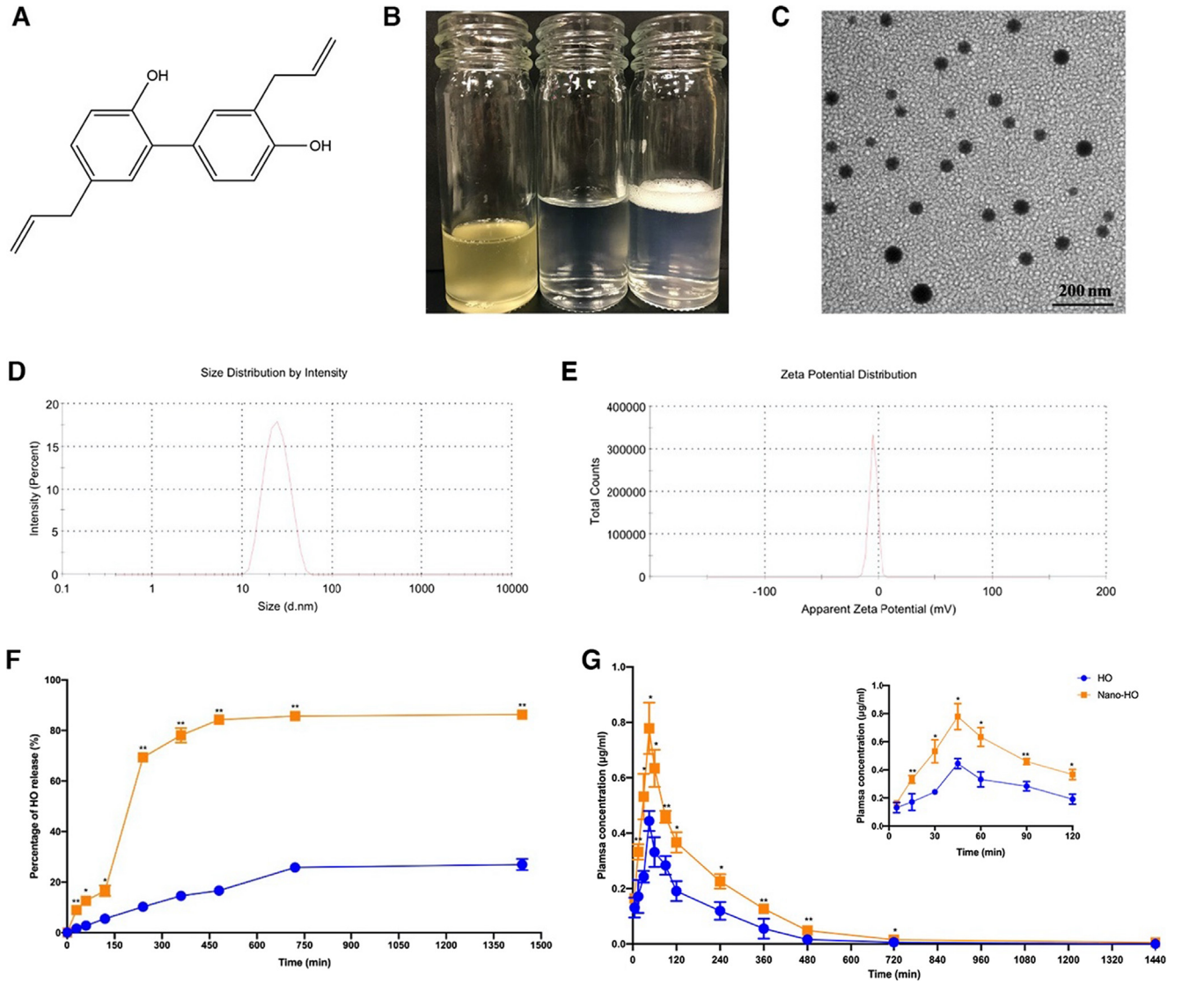

Fig. 1. (A) Chemical structure of HO. (B) Appearance of the Nano-HO as stocking solution (a) as working solution that diluted 100-fold with distilled water; (b) HO solution that suspended in 0.5% CMC-Na (c). (C) TEM image of Nano-HO droplet. (D) Particle size and distribution of Nano-HO. (E) ZP of Nano-HO. (F) *In vitro* release of Nano-HO and HO in PBS (pH 7.4). (G) Plasma concentration–time profiles of rats after oral administration with Nano-HO (80 mg/kg) and HO (80 mg/kg). Data are expressed as mean ± SEM (n = 5). * $p < 0.05$ and ** $p < 0.01$ as compared with free HO group.

Preparation of Nano-HO

Nano-HO was prepared using Kolliphor® HS-15 (surfactant), PEG-400 (co-surfactant), and MCT (oil) at the ratio of 4:2:1 (w/w/w). HO was dissolved in MCT, then mixed with HS-15 and PEG-400, followed by gently stirring using a magnetic stirrer at 300 rpm for 30 min at 25 °C. After equilibrium at room temperature, the solution was diluted 100-fold with double-distilled water and stirred till clear and slightly bluish.

Characterization of Nano-HO

The droplet size, zeta potential (ZP) and poly-dispersity index (PDI) were measured at 25 °C by a Zetasizer Nano ZS (Malvern Instruments, UK) based on dynamic light scattering. The morphology of Nano-HO was determined by Hitachi-HT7700 transmission electron microscope (Hitachi-Technologies Corp., Tokyo, Japan). Samples with a 500-fold dilution were placed on a copper grid (400 mesh). After the samples were dried, they were stained with phosphotungstic acid (2%) for 30 s at room temperature to form a thin film, and then observed under transmission electron microscope (TEM).

In vitro release of Nano-HO and HO

The *in vitro* release of Nano-HO and HO was determined by a modified method described previously [14]. Briefly, 5 mL of Nano-HO (containing 5 mg HO) and HO (5 mg HO suspended in 0.5% CMC-Na as control) were placed into a dialysis bag (molecular weight cut-off of 8000–14000 Da) immersed in 100 mL of phosphate-buffered saline (PBS, pH 7.4) and incubated at 37 °C in a SHA-B double-functional thermostat water bath vibrator (Changzhou Aohua Instrument Co., Ltd, Jiangsu, China) at 100 rpm/min. Two hundred microliter of dialysates were collected at 0, 30, 60, 120, 240, 360, 480, 720 and 1440 min, while the same volume of fresh PBS (37 °C) was subsequently added into the dialysis solution. After centrifugation at 10000 rpm for 10 min, the dialysates were collected and passed through a 0.22 μm filter. The contents of HO in the dialysis buffer were quantified by HPLC while

a standard curve was made for titration. For HPLC analysis, the samples were sonicated in 0.2 mL of methanol and detected three times by normalizing the results against the standard curve of HO. The analysis was performed using a Shimadzu SIL-20 AHPLC system. The isocratic mobile phase was performed with the mixture of methanol and distilled water (76:24, v/v) at a flow rate of 1.0 mL/min on a unisol C_{18} column (5 μm, 100 A°, 4.6 × 250 mm, Agela Technologies, Tianjin, China). The column temperature was set at 40 °C and detection wavelength was at 294 nm. The HO released from Nano-DDS and free HO by percentages were plotted against time.

Animals

Male Sprague Dawley (SD, weighing 230–250 g) rats were obtained from the Laboratory Animal Services Centre, Guangzhou University of Chinese Medicine. Male TgCRND8 mice were crossed with female non-transgenic mice on the hybrid C3H/He-C57BL/6 background to breed a colony of experimental animals. Non-transgenic littermates that did not express human APP transgene were identified as wild-type mice and used as negative control for experiments. Both rats and mice were maintained on a 12 h light/dark cycle under controlled humidity (50 ± 10%) and temperature (24 ± 2 °C), with access to food and water *ad libitum*. Since the housing condition markedly influenced the emotional and depression-like behaviors of the male mice, in the present study, the male mice were group rearing (3 mice per cage). The experimental procedures used in the present study were in compliance with the ARRIVE guidelines and carried out in accordance with the National Institutes of Health guide for the care and use of Laboratory animals.

Pharmacokinetics study

After acclimatization, male SD rats (weighing 230–250 g) were randomly assigned into Nano-HO group and HO group (n = 5) and administrated orally with the same content of HO (80 mg/kg). The dosage of HO was selected based on a previous report [14]. Afterwards, the rat blood samples (0.30 mL each) were collected at 5, 15, 30, 45, 60, 90, 120, 240, 360, 480, 720, and 1440 min from the rat eye socket veins via heparinized capillary tubes under anesthetization with diethyl ether. After centrifugation at 3500 rpm for 10 min at 4 °C, plasma samples were collected and stored at −20 °C for further analysis. The plasma sample preparation was carried out based on a previously described method [14]. Briefly, 200 μL plasma was mixed with 50 μL docetaxel (800 μg/mL, internal standard) and 350 μL methanol in a vortex mixer for 30 s. The mixture was centrifuged at 12000 rpm for 15 min at 4 °C. Then, all supernatants were transferred to the auto-sampler vials for introduction into the HPLC system. The conditions of HPLC analysis were identical to that described in the "*In vitro* release of Nano-HO and HO" section.

Analysis software DAS (Version 3.0; Data Analysis System, Shanghai, China) was used to assess the pharmacokinetic parameters according to the non-compartmental model. With the concentration time curve ranging from 0 to 24 h (AUC_{0-24}), the maximum plasma concentration (C_{max}), and peak time (T_{max}) were obtained directly from the plasma concentration vs time curve. The mean residence time (MRT_{0-24}), and the biological half-life time ($t_{1/2}$) were estimated from the terminal linear portion of the plasma concentration–time profile. The relative bioavailability was calculated as:

$$\text{Relative bioavailability} = AUC_{0--24}\text{of Nano} - \text{HO}/AUC_{0--24}\text{of pure HO} * 100\%.$$

Polymerase chain reaction (PCR) for genotyping

All mice were subjected to genotyping for the APP transgene before experiments as described in our previous study [15]. PCR analysis was performed on genomic DNA isolated from ear using the following primers: Forward- TGTCCAAGATGCAGCAGAACGGC-TAC, Reverse - AAACGCCAAGCGCCGTGACT. Those mice with APP transgene were identified as transgenic mice, while those without APP transgene as wild type (WT) ones.

Experimental design and drug treatment in TgCRND8 mice

Three-month-old male mice were divided into 5 groups with 9 mice in each group: (1) WT group; (2) TgCRND8 (Tg) + vehicle group; (3) Tg + HO (20 mg/kg) group; (4) Tg + Nano-HO (20 mg/kg) group; (5) Tg + Donepezil (5 mg/kg) group. The dosage of HO was selected based on the previous studies [9,16]. Donepezil was chosen as a positive control and dissolved in normal saline. HO was suspended in 0.5% CMC-Na. Mice were administered with HO, Nano-HO and donepezil by gavage once daily for 17 consecutive weeks, whereas mice in the WT group and Tg+ vehicle group received the same volume of vehicle (blank-Nano-formation) for the same duration. After drug treatment, the spatial learning and memory functions were assessed by Morris Water Maze test (MWMT). Fig. 2A showed the experimental design and drug treatment schedule.

Morris water maze test (MWMT)

The modular MWMT with a video tracking software of Super-Maze V2.0 was purchased from Xinruan Information Technology Co. Ltd (Shanghai, China). A tank was acted as a maze, and the diameter and the height of the maze were 180 and 70 cm, respectively. The tank was located in a test room that contained various prominent visual color pictures (e.g., Triangle, circle, quadrate, etc.). The maze was filled with water at 25 °C and divided into four equal quadrants. A circular escape platform with 10 cm of diameter was fixed in the midpoint of one quadrant and submerged 2 cm below the water surface. The mice were trained to find the hidden platform for consecutive 4 days. There were 3 trials for each mouse per day, and the inter-trial interval of each trial was 60 s. To minimize the performance differences caused by circadian rhythmicity, the MWMT was performed between 9:00 and 18:00. In each trial, we placed the mice gently in one quadrant randomly with its nose pointing toward the wall and allowed them to find the escape platform. Each mouse was given 60 s to find the platform and allowed to stay on it for 30 s. If a mouse did not find the platform within 60 s, the mouse was gently guided to platform and allowed it to stay on the platform for 30 s before the next trial, and the escape latency (the time for finding the submerged platform) was recorded as 60 s. To determine the ability of spatial learning, the time of the mouse spent to reach the platform was recorded, and the mean value of the three trials was calculated. On day 5, the probe test of spatial memory was conducted by removing the platform and allowing each mouse to swim freely for 60 s. The time spent in the target quadrant (where the platform was once hidden) and the number of crossings through the platform quadrant were recorded.

Brain sample processing

Twenty-four h after MWMT, 6 mice in each group were euthanized with ketamine and xylazine, then the brain tissues were removed rapidly and separated into two hemispheres equally for western blotting analysis and ELISA assay. All samples were stored at − 80 °C before further analysis. For immunofluorescence analy-

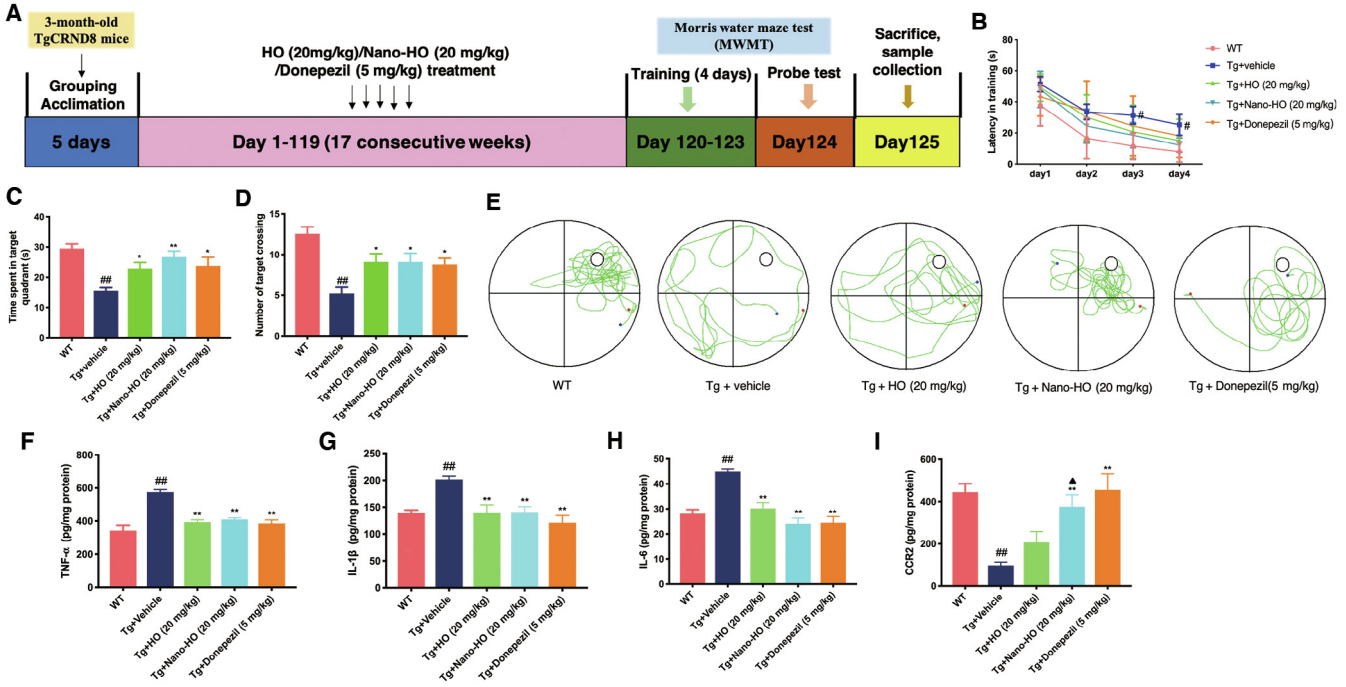

Fig. 2. Nano-HO improved the spatial learning and memory functions of TgCRND8 mice. The spatial learning and memory functions were evaluated using MWMT (n = 9). (A) Experimental design and treatment schedule to evaluate the neuroprotective effects of HO and Nano-HO on TgCRND8 transgenic mice; (B) The latency to find a hidden platform during 4 consecutive days of training; (C) Time spent in the target quadrant; (D) Number of target crossings; (E) Representative swimming tracks of mice in the probe test. Nano-HO decreased the levels of cytokines including TNF-α (F), IL-1β (G) and IL-6 (H), enhanced the level of CCR2 (I) in the brain tissues of TgCRND8 mice (n = 6). Data were expressed as mean ± SEM. $^{\#}$ $p < 0.05$ and $^{\#\#}$ $p < 0.01$ when compared with the WT group; * $p < 0.05$ and ** $p < 0.01$ when compared with the Tg + vehicle group; ▲ $p < 0.05$ when compared with free HO group.

sis, 3 mice in each group were deeply anesthetized using xylazine and ketamine and transcardially perfused with 0.9% saline followed by buffered 4% paraformaldehyde. Afterwards, the brain tissues were post-fixed in 4% paraformaldehyde overnight at 4 °C, then stored in 30% sucrose at 4 °C until sectioned.

Ethics statement

All experiments involving animals were conducted according to the ethical policies and procedures approved by the Animal Experimentation Ethics Committee of The Chinese University of Hong Kong (Ref. No. 18/108/GRF).

Cytokine determination

The brain tissues of mice were homogenized vigorously in 0.8 mL of lysis buffer (contained in the kits). After incubation on ice for 20 min, the homogenates were centrifuged at 12000 rpm for 20 min at 4 °C. Protein concentrations were determined by Pierce™ BCA protein assay kit (Catalog no.: 23227, Thermo Fisher Scientific). The levels of TNF-α (Catalog no.: ab100747, Abcam, Cambridge, UK), IL-6 (Catalog no.: ab100712, Abcam, Cambridge, UK), IL-1β (Catalog no.: ab100704, Abcam, Cambridge, UK) and CCR2 (Catalog no.: CSB-EL004841MO, CUSABIO, Houston, USA) in the supernatants were determined using commercially available ELISA kits according to the manufacturer's instructions. The levels of TNF-α, IL-6, IL-1β and CCR2 were expressed as pg/mg protein.

Western blotting

For preparation of protein lysates, frozen brain tissues were homogenized in RIPA lysis buffer (Catalog no.: 89900, Thermo Fisher Scientific) which contains 1% protease/phosphatase inhibitor cocktail (Catalog no.: 78442, Thermo Fisher Scientific) for 30 min on ice. After centrifugation at 14,000 rpm at 4 °C for 15 min, the supernatants were collected. Protein concentrations were determined by Pierce™ BCA protein assay kit (Catalog no.: 23227, Thermo Fisher Scientific). Equal amounts of proteins of different samples were loaded. The proteins were separated by SDS-PAGE and then transferred to PVDF membranes. After being blocked with 5% (w/v) non-fat milk in TBST at room temperature for 2 h, the PVDF membranes were incubated at 4 °C overnight with primary antibodies against CTFs (1:1000; Catalog no.: A8717, Sigma), p-APP (Thr688) (1:1000; Catalog no.: 6986S, Cell Signaling Technology), BACE-1 (1:1000; Catalog no.: SAB2100200, Sigma), APH-1 (1:1000, Catalog no.: PRS4001, Sigma), PS-1 (1:500; Catalog no.: sc-365450, Santa Cruz), IDE (1:500; Catalog no.: sc-393887, Santa Cruz), NEP (1:1000; Catalog no.: AP1126-SP, R&D Systems), p-Tau (Thr 205) (1:500; Catalog no.: sc-101817, Santa Cruz), p-Tau (Ser 396) (1:1000; Catalog no.: ab109390, Cell Signaling Technology), p-Tau (Ser 404) (1:1000; Catalog no.: ab92676, Cell Signaling Technology), tau (Tau 46) (1:500; Catalog no.: sc-32274, Santa Cruz), caspase-3 (1:500; Catalog no.: sc-7148, Santa Cruz), B cell lymphoma-2 (Bcl-2) (1:500; Catalog no.: sc-7382, Santa Cruz), p-JNK (1:500; Catalog no.: sc-12882, Santa Cruz), JNK (1:500; Catalog no.: sc-7345, Santa Cruz), p-GSK-3β (Ser 9) (1:1000 Catalog no.: 9336 s, Cell Signaling Technology), GSK-3β (1:500; Catalog no.: sc-9166, Santa Cruz), CDK5 (1:1000; Catalog no.: 2506, Cell Signaling Technology), p35/25 (1:1000; Catalog no.: 2680, Cell Signaling Technology) and β-actin (1:500; Catalog no.: sc-69879, Santa Cruz). After rinsing with TBST for 5 min × 3 times, the PVDF membranes were then incubated with secondary antibodies against anti-mouse (1:1000; Catalog no.: 7076 s, Cell Signaling Technology), anti-rabbit (1:1000; Catalog no.: 7074 s, Cell Signaling Technology) and donkey anti-goat (1:1000; Catalog no.: sc-2020, Santa Cruz) for 2 h at room temperature. After rinsing with TBST for 5 min × 3 times,

the protein bands were visualized by the Pierce™ ECL western blotting substrate (Catalog no.: 32106, Thermo Fisher Scientific). The intensity of each band was imaged by acer c300 (Azure systems, Mumbai, India) and analyzed using Image J software (NIH Image, MD, USA).

Immunofluorescence assay

Coronal brain sections were sectioned at a thickness of 30 μm using cryostat (Leica CM1850, Leica Microsystems GmbH, Wetzlar, Germany) and stored at 4 °C in 0.1 M PB. Prior to staining, the sections were immersed in 0.25% trypsin and incubated at 37 °C for 30 min to achieve antigen retrieval. Then the sections were rinsed in PB three times for 15 min, followed by permeabilization in 0.1 M PB solution with 0.3% Triton, and subsequently incubated overnight at room temperature on a shaker with primary antibodies against anti-β-amyloid 17–24 antibody (1:500; Catalog no.: A5213, Sigma, USA), anti-GFAP polyclonal antibody (1:500; Catalog no.: HPA056030, Sigma, USA) and anti-IBA-1 antibody (1:500; Catalog no.: 019–19741, Wako, Japan) in the blocking solution. On the following day, the sections were rinsed with PB three times for 15 min. Next, the sections were incubated with donkey anti-mouse secondary antibody conjugated with Alexa Fluor 488, donkey anti-rabbit secondary antibody conjugated with Alexa Fluor 594 and donkey anti-mouse secondary antibody conjugated with Alexa Fluor 647 (1:500) (Life Technology/Thermo Fisher Scientific, Waltham, MA) for 2 h at room temperature in dark, followed by rinsing with PB three times for 15 min. The sections were then mounted on microscope slides (Lab'IN Co, NT, Hong Kong) and cover-slipped using fluorescence mounting medium (Dako North America, Inc., CA, USA). Immunofluorescent images were captured using a Zeiss fluorescent inverted microscope (Zeiss, Gottingen, Germany) equipped with an ORCA-Flash 4.0 v2 digital CMOS camera (Hamamatsu Photonics, Iwata City, Japan). The quantification was analyzed by two investigators who were blinded to the animal grouping using Image J software (NIH, Bethesda, MD, USA) according to previous reports [17,18].

Fecal DNA extraction and Illumina miseq sequencing

Fecal samples of the mice were collected into 2 mL tubes and stored at −80 °C after frozen in liquid nitrogen. Fecal genomic DNA was extracted with OMGA-soil DNA kit as per the manufacturer's instruction. Hypervariant region V4 of bacterial 16S rRNA gene was amplified with the forward primer 515F (5′-GTGCCAGC MGCCGCGGTAA-3′) and reverse primer 806R (5′-GGAC TACHVGGGTWTCTAAT-3′) by PCR. Products were purified with Agencourt Ampure XP beads (AGENCOURT, Beckman coulter, US) to remove the unspecific products. The quality of sequencing library was analyzed by Agilent 2100 bioanalyzer instrument (Agilent DNA 1000 Reagents, CA, USA) to determine the average molecular weights. Purified amplicons were sequenced pair end on the Illumina MiSeq PE300 System at Beijing Genomics Institute. Raw fastq files were quality-filtered using QIIME61 (v1.17). The taxonomy of each sequence was analyzed by RDP Classifer (v2.2) against Silva (v119) 16S rRNA database with 80% confidence threshold. Rarefaction analysis was performed by Mothur (v1.31.2) and α-diversity indexes were compared using rarefed data. Principal component analysis (PCA) plot was implemented by R programming language.

Statistical analysis

All data were presented as the mean ± SEM. The comparative *t*-test was applied using SPSS software to assess the statistical significance in the pharmacokinetic study. Group differences in the escape latency in the Morris water maze training task were analyzed using two-way analysis of variance (ANOVA) with repeated measures, with the factors being treatment and training day. The other data were analyzed using one-way ANOVA followed by Post-hoc Bonferroni's test to detect inter-group differences. Group differences between HO group and Nano-HO group were analyzed using a two-tailed student's *t*-test. GraphPad Prism software (Version 8, GraphPad Software, Inc., CA, USA) was used to perform the statistical analysis. A difference was considered statistically significant when the $p < 0.05$.

Results

Physicochemical properties, in vitro drug release and pharmacokinetics study of Nano-HO

As shown in Fig. 1B a-c, Nano-HO was a transparent viscous liquid at room temperature and formed a clear and transparent microemulsion after diluting with 100-fold distilled water. When the same content of HO was suspended in 0.5% CMC-Na solution, it was white turbid liquid. The morphology of Nano-HO was observed under TEM (Fig. 1C), and it was displayed as microemulsion droplets that were nearly spherical with a small size and dispersed homogeneously in aqueous medium. Fig. 1D-E showed that the mean droplet size of Nano-HO was 23.30 ± 0.46 nm with PDI of 0.087 ± 0.00, and the average ZP of Nano-HO was − 6.19 ± 1.70 mV.

The *in vitro* release results demonstrated that HO and Nano-HO were gradually released into the dialysis buffer over a period of 24 h (Fig. 1F). The accumulative release rate of Nano-HO (86.3%) was significantly higher than that of regular HO (27.0%) ($p < 0.01$). As shown in Fig. 1G and Table 1, our pharmacokinetics results demonstrated that the T_{max} was similar in Nano-HO (0.79 5 ± 0.102 h) and HO (0.758 ± 0.041 h), and the half-life ($t_{1/2}$) of Nano-HO (2.169 ± 0.281 h) was prolonged about 1.82-fold as compared to that of HO (1.189 ± 0.232 h). Moreover, the peak concentration (C_{max}) of Nano-HO (0.779 ± 0.093 μg/mL) was enhanced nearly 1.75-fold than that of HO (0.444 ± 0.016 μg/mL) ($p < 0.05$). The mean residence time (MRT_{0-24}) of Nano-HO (3.465 ± 0.143 h) was significantly longer than that of the HO (2.909 ± 0. 132 h) ($p < 0.05$). The area under the concentration–time curves from 0 to 24 h (AUC_{0-24}h) of Nano-HO and HO were 2.366 ± 0.07 9 μg·h/ mL and 1.232 ± 0.066 μg·h/ mL respectively, yielding a relative bioavailability of 192.045% ($p < 0.01$) for Nano-HO.

Nano-HO improved cognitive deficits in TgCRND8 mice

Fig. 2B showed a significant difference in the mean latency during pre-training stage between training days ($F(3, 160) = 40.80$, $p < 0.001$) and between treatments ($F(4, 160) = 7.319$, $p < 0.001$).

Table 1
Pharmacokinetics parameters after oral administration with Nano-HO (80 mg/kg) and HO (80 mg/kg).

Parameters	HO	Nano-HO
AUC_{0-12} (μg·h/ mL)	1.232 ± 0.066	2.366 ± 0.079**
$t_{1/2}$ (h)	1.189 ± 0.232	2.169 ± 0.281
T_{max} (h)	0.758 ± 0.041	0.795 ± 0.102
C_{max} (μg/mL)	0.444 ± 0.016	0.779 ± 0.093*
MRT_{0-12} (h)	2.909 ± 0.132	3.465 ± 0.143*
Relative bioavailability (%)	–	192.045%

Data are expressed as mean ± SEM (n = 5).
* $p < 0.05$.
** $p < 0.01$ as compared with HO group.

Mice in Tg + vehicle group exhibited prolonged escape latency compared with WT mice from day 3 ($F(4, 40) = 2.234$, $p < 0.05$) and day 4 ($F(4, 40) = 2.262$, $p < 0.05$), which means that TgCRND8 mice spent more time to find the platform, indicating a spatial learning deficit in TgCRND8 mice. Whereas the escape latency was improved after drug intervention when compared with the TgCRND8 group. Fig. 2C-E showed severe deficits in spatial memory formation of TgCRND8 mice, as indicated by less time staying in the target quadrant ($F(4, 40) = 7.139$, $p < 0.001$) and fewer crossings of the hidden platform ($F(4, 40) = 8.340$, $p < 0.001$) than WT mice in the probe test. Mice in HO and Nano-HO groups spent more time in the target quadrant ($p < 0.05$ and $p < 0.01$ respectively) and had increased frequency of platform crossing ($p < 0.05$ for both) when compared to TgCRND8 mice.

Nano-HO modulated inflammatory cytokines and chemokine

As shown in Fig. 2F-H, the levels of TNF-α ($F(4, 25) = 20.59$, $p < 0.001$), IL-1β ($F(4, 25) = 8.208$, $p < 0.001$) and IL-6 ($F(4, 25) = 18.46$, $p < 0.001$) in the brain tissues of TgCRND8 mice were markedly increased, as compared with WT group. Nano-HO treatment significantly suppressed the productions of TNF-α ($p < 0.01$), IL-1β ($p < 0.01$) and IL-6 ($p < 0.01$) as compared with the Tg + vehicle group. In addition, the level of CCR2 ($F(4, 25) = 9.272$, $p < 0.001$) in the brain tissues of TgCRND8 mice was significantly decreased, as compared with WT group. Nano-HO treatment more potently elevated the production of CCR2 than free HO group ($p < 0.05$), as compared with the Tg + vehicle group ($p < 0.01$).

Nano-HO inhibited Aβ plaque-associated neuroinflammation

As shown in Fig. 3A, significant increase in the microglia density was observed in the hippocampus ($F(4, 20) = 64.65$, $p < 0.001$) and the cortex ($F(4, 20) = 54.31$, $p < 0.001$) of TgCRND8 mice, as compared with the WT group. Nano-HO treatment markedly decreased the microglia density both in the hippocampus ($p < 0.01$ for both) and cortex ($p < 0.01$ for both) of TgCRND8 mice. In addition, there were marked increase in the astrocyte density in the hippocampus ($F(4, 20) = 83.18$, $p < 0.001$) and cortex ($F(4, 20) = 72.22$, $p < 0.001$) in TgCRND8 mice, when compared with the WT group (Fig. 3B). Nano-HO treatment significantly attenuated the astrocyte density both in the hippocampus ($p < 0.01$ for both) and cortex ($p < 0.05$ and $p < 0.01$, respectively). Interestingly, our results also revealed that microglia cells had a larger cell area and a larger cell perimeter in TgCRND8 mice, as compared with the WT control group. However, the microglia cells in Nano-HO or free HO treatment groups showed reduced cell area and cell perimeter of the microglia cells in the hippocampus and cortex. Microglia cells usually had rod or fusiform shape and less stellate shape and branching in the hippocampus and cortex of the control group, while they showed increased astrocytic branching with more stellate shape in the hippocampus and cortex of the Tg+ vehicle control group. Nano-HO or free HO treatment could decrease the astrocytic branching and the number of the microglia cells with stellate shape. Furthermore, Aβ plaque burdens were significantly elevated in the hippocampus ($F(4, 20) = 45.68$, $p < 0.001$) and the cortex ($F(4, 20) = 124.6$, $p < 0.001$) of TgCRND8 mice, as compared with the WT mice (Fig. 3C). The Aβ plaque burdens in Nano-HO group were significantly decreased in the hippocampus ($p < 0.01$ for both) and the cortex ($p < 0.01$ for both). Notably, Nano-HO more markedly decreased the astrocyte density both in the hippocampus ($p < 0.01$) and the cortex ($p < 0.01$), and reduced the Aβ plaque burdens in the hippocampus ($p < 0.05$) of TgCRND8 mice than regular HO.

Nano-HO modulated APP processing, suppressed tau protein hyperphosphorylation and regulated JNK/CDK5/GSK-3β signaling pathway

As shown in Fig. 4A, the protein expressions of CTFs ($F(4, 20) = 79.20$, $p < 0.001$), p-APP (Thr 688) ($F(4, 20) = 15.77$, $p < 0.001$), BACE-1 ($F(4, 20) = 9.205$, $p < 0.001$), APH-1 ($F(4, 20) = 16.79$, $p < 0.001$) and PS-1 ($F(4, 20) = 7.305$, $p < 0.001$) were significantly augmented, while the protein expressions of IDE ($F(4, 20) = 14.50$, $p < 0.001$) and NEP ($F(4, 20) = 20.66$, $p < 0.001$) were markedly attenuated in the brain tissues of TgCRND8 mice. Treatment with Nano-HO significantly mitigated the protein expressions of p-APP (Thr 688) ($p < 0.05$ and $p < 0.01$, respectively), BACE-1 ($p < 0.01$ for both), APH- 1 ($p < 0.01$ for both) and PS-1 ($p < 0.01$ for both) of TgCRND8 mice. Furthermore, Nano-HO significantly accentuated the protein expressions of IDE ($p < 0.01$) and NEP ($p < 0.01$) of TgCRND8 mice, while HO treatment did not affect the protein expressions of IDE and NEP. In addition, Nano-HO was more effective than HO in inhibiting the protein expressions of p-APP and BACE-1 (both $p < 0.05$), as well as enhancing the expressions of NEP ($p < 0.01$) of TgCRND8 mice.

The protein expression level of caspase-3 ($F(4, 20) = 18.25$, $p < 0.001$) of TgCRND8 was significantly elevated, while Bcl-2 expression ($F(4, 20) = 15.98$, $p < 0.001$) was decreased, when compared with the WT group (Fig. 4B, respectively). After treatment with Nano-HO, the expression of caspase-3 was effectively mitigated ($p < 0.01$). In addition, Nano-HO treatment also significantly increased the Bcl-2 expression ($p < 0.01$), when compared with the Tg + vehicle group. As shown in Fig. 4C, the ratios of p-Tau (Thr 205)/Tau (46) ($F(4, 20) = 13.25$, $p < 0.001$) and p-Tau (Ser 404)/Tau (46) ($F(4, 20) = 5.133$, $p < 0.01$) were markedly increased in TgCRND8 mice, which were significantly down-regulated by Nano-HO treatment ($p < 0.05$, $p < 0.01$ respectively). However, no significant differences were found among all groups in the expressions of p-Tau (Ser 396) ($F(4, 20) = 0.4475$, $p > 0.05$). Notably, Nano-HO was more effective than HO in attenuating the ratio of p-Tau (Thr 205)/Tau (46) ($p < 0.05$).

As clearly shown in Fig. 4C, as compared to the WT group, the ratio of p-JNK/JNK was significantly up-regulated in the Tg + vehicle group ($F(4, 20) = 22.79$, $p < 0.001$). Nano-HO treatment was able to down-regulate the ratio of p-JNK/JNK ($p < 0.01$). Additionally, significant increase in the ratio of p-35/CDK5 ($F(4, 20) = 10.16$, $p < 0.001$) was observed in the Tg + vehicle group, which was remarkably attenuated by Nano-HO treatment ($p < 0.01$). On the other hand, the ratio of p-GSK-3β (Ser9)/GSK-3β was markedly decreased in TgCRND8 mice ($F(4, 20) = 13.37$, $p < 0.001$). Nano-HO treatment markedly increased the ratio of p-GSK-3β (Ser9)/GSK-3β ($p < 0.01$). In addition, Nano-HO showed more potency in suppressing the ratio of p-JNK/JNK ($p < 0.05$) and p-35/CDK5 ($p < 0.01$), and inhibiting the activation of GSK-3β via elevating the ratio of p-GSK-3β (Ser9)/GSK-3β ($p < 0.01$) than free HO.

Gut microbiota composition at different levels among groups

The system clustering tree (Fig. 5A) revealed that mice in HO and Nano-HO groups were clustered separately from Tg + vehicle group, reflecting that HO and Nano-HO caused the changes of gut microbiota in TgCRND8 mice.

For α-diversity analysis, the Shannon index was significantly decreased and Simpson index was remarkably increased in TgCRND8 mice (Fig. 5B-C). Nano-HO treatment improved the Shannon index, and significantly decreased the Simpson index, indicating that Nano-HO could improve the diversity and species evenness in the fecal samples of TgCRND8 mice.

Additionally, principal coordinate analysis (PCoA) and partial least squares discrimination analysis (PLS-DA) both yielded well

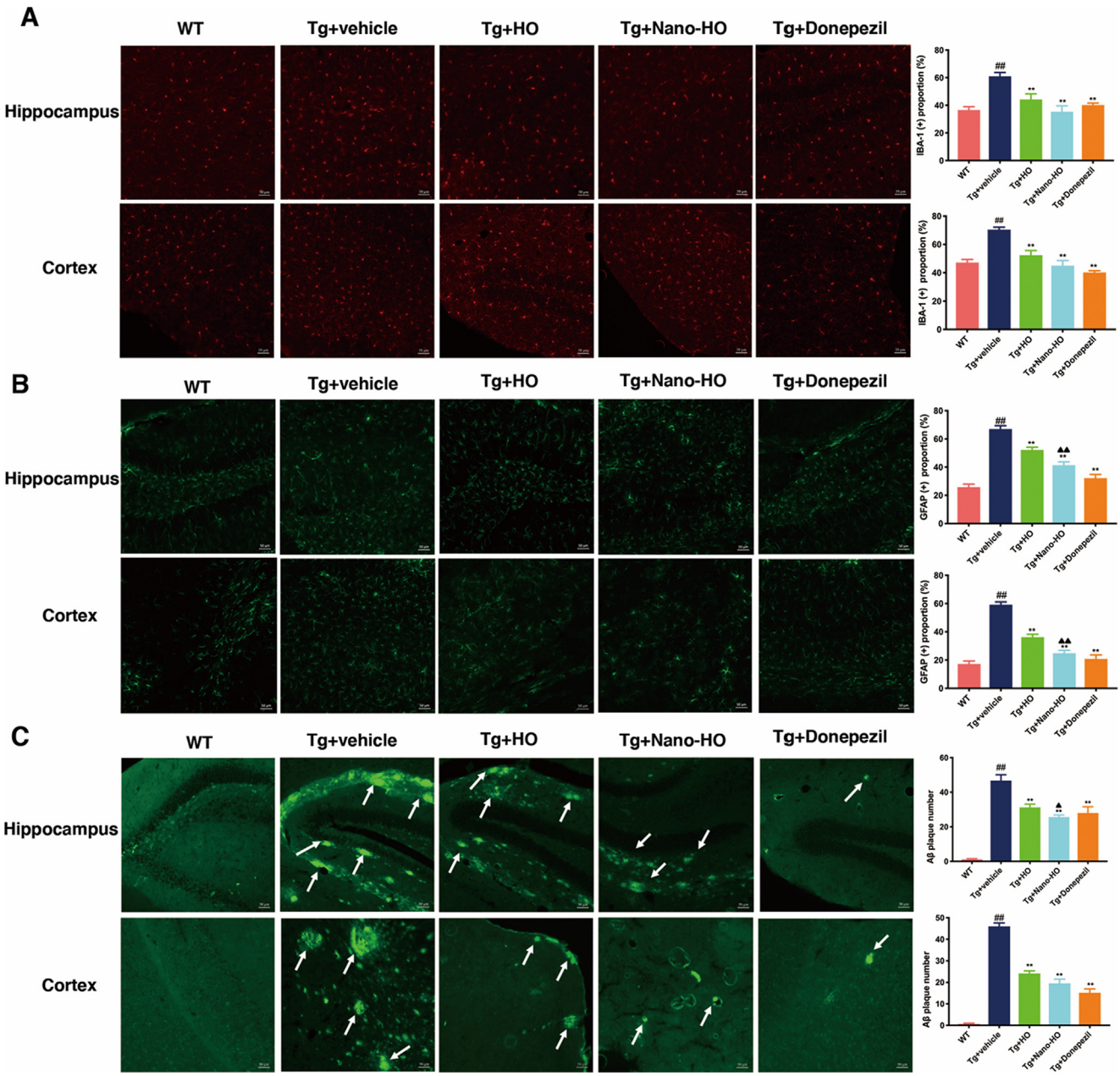

Fig. 3. Nano-HO attenuated Aβ deposition and Aβ plaque-associated neuroinflammation. Microglia (B), Astrocytes (C) and Aβ deposits (D) in the hippocampus and cortex of TgCRND8 mice were presented respectively. Magnification: 200*. Data were expressed as mean ± SEM (n = 5). $^{\#\#}$ $p < 0.01$ when compared with WT group; * $p < 0.05$ and ** $p < 0.01$ when compared with Tg + vehicle group; ▲ $p < 0.05$ and ▲▲ $p < 0.01$ when compared with HO group.

separated positions among the groups (Fig. 5D-E). Notably, the bacterial communities in the Nano-HO group were more closely clustered with WT mice than HO group, which differed from TgCRND8 mice, suggesting that the bacterial communities were altered in the Nano-HO treated mice.

Fig. 5F-J illustrated the gut microbiota community composition and dominant bacterial distribution at different levels in fecal samples. At the phylum level, the most abundant phyla were *Bacteroidetes, Firmicutes, Proteobacteria,* accounting for 90% of the total microbiome composition, followed by *Cyanobacteria-1*, *Deferribacteria* and *Actinobacteria* (supplementary Fig. 2A). The proportion of *Firmicutes* was decreased by 59.0%, while *Bacteroidetes* and *Proteobacteria* were increased by 186.6% and 278.0%, respectively, in Tg + vehicle group, when compared the WT group (Fig. 5F). Nano-HO treatment showed better effect on returning the proportions of *Deferribacteria* and *Actinobacteria* than that of HO.

At the class level, 16 genera were identified (supplementary Fig. 2B). The relative abundance of *Bacillus*, *α-Proteobacteria*, *β-Proteobacteria*, *δ-Proteobacteria* and *ε-Proteobacteria* were significant higher, while the proportion of *Erysipelotrichi* was significantly lower in TgCRND8 mice (Fig. 5G). Nano-HO treatment reversed the proportions of *Erysipelotrichi, ε-Proteobacteria* and *α-Proteobacteria* in TgCRND8 mice in a more effectively manner than HO.

At the order level, 19 genera were identified (supplementary Fig. 2C). *Clostridiales* was of predominance in all samples among five groups and showed a high abundance in the Tg + vehicle group (Fig. 5H). The relative abundance of *Campylobacterales* and *Desulfovibrionales* was significantly higher, whereas the relative abundance of *YS32* and *Bifidobacteriales* was remarkably decreased in

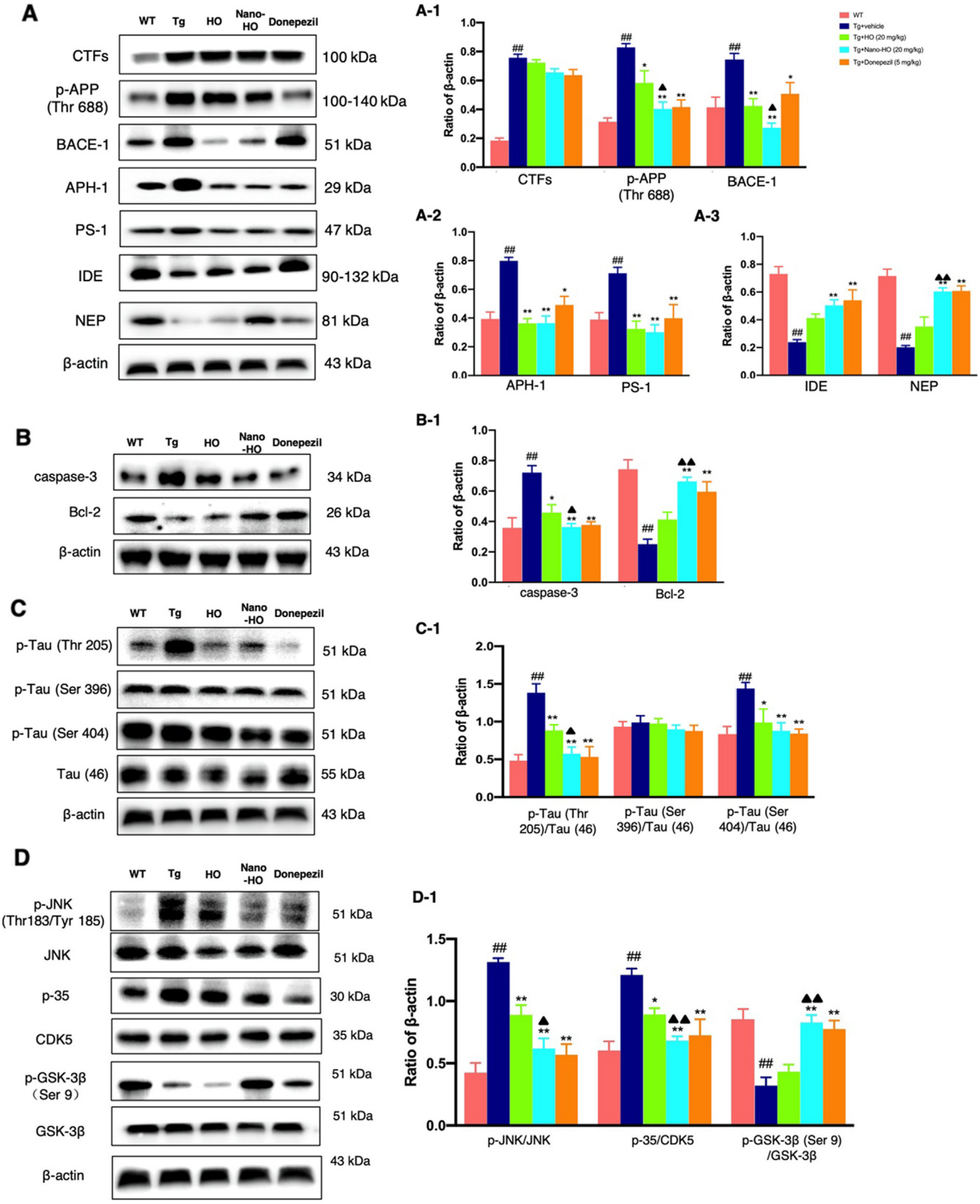

Fig. 4. Nano-HO modulated the APP phosphorylation, suppressed apoptosis and tau hyperphosphorylation, and modulated JNK/CDK5/GSK-3β signaling pathway in the brain tissues of TgCRND8 mice. (A) Representative western blotting images and quantitative analysis of the protein expressions of CTFs, p-APP (Thr 688), BACE-1, APH-1, PS-1, IDE and NEP; (B) Representative western blotting images and quantitative analysis of the caspase-3 and Bcl-2 protein expressions; (C) Representative western blotting images and quantitative analysis of the p-Tau (Thr 205), p-Tau (Ser 396), p-Tau (Ser 404) and tau (Tau 46) protein expressions; (D) Representative western blotting images of the protein expressions and quantitative analysis of p-JNK, JNK, p-35, CDK5, p-GSK-3β (Ser 9) and GSK-3β. Data were expressed as mean ± SEM (n = 5). $^{\#\#}$ $p < 0.01$ when compared with the WT group; * $p < 0.05$ and ** $p < 0.01$ when compared with the Tg + vehicle group; ▲ $p < 0.05$ and ▲▲ $p < 0.01$ when compared with HO group.

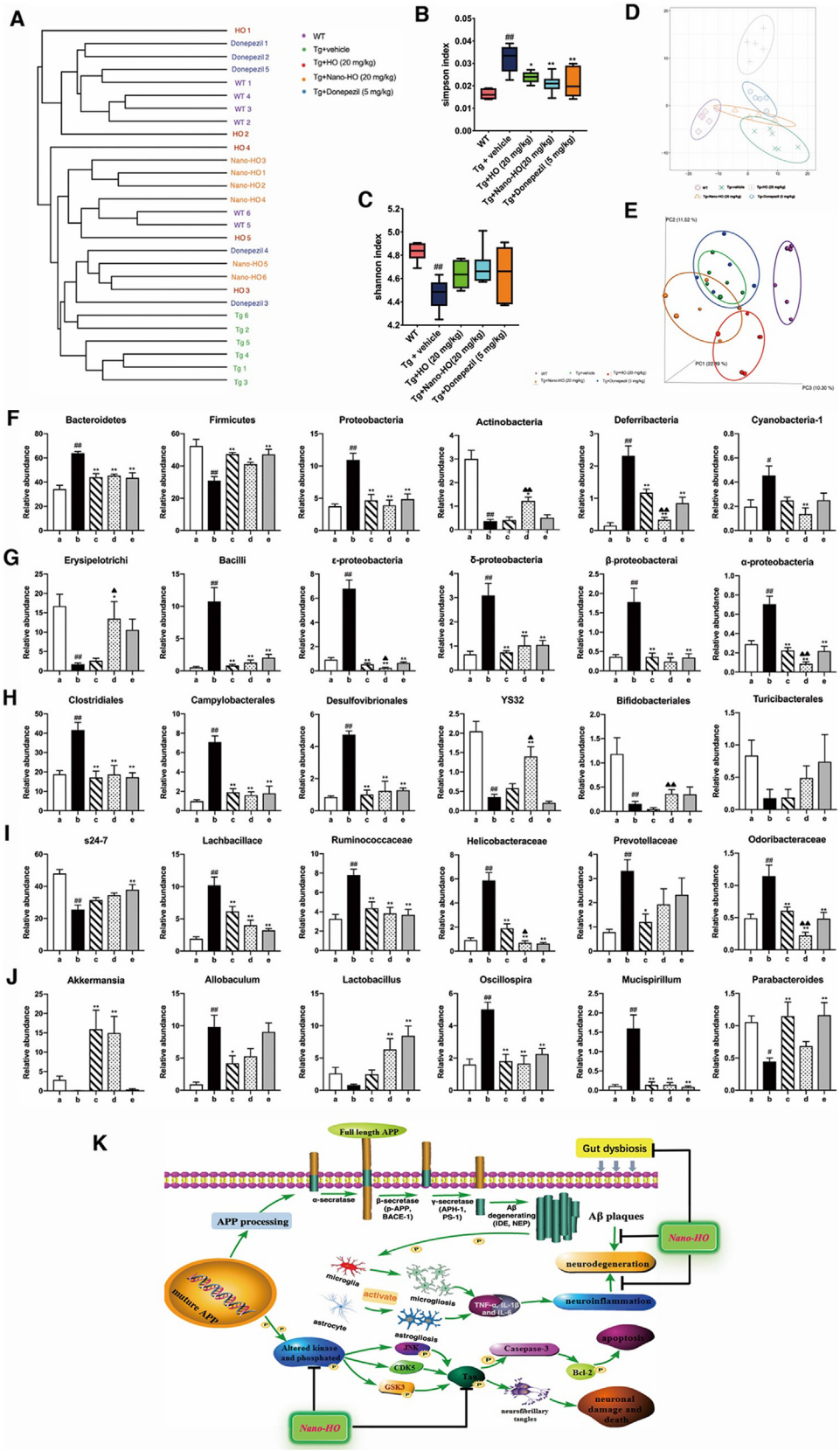

Fig. 5. (A) The system clustering tree. (B,C) α-diversity analysis (Shannon index and Simpson index). (D) PCoA analysis of gut bacteria (PC1 versus PC2). (E) PLS-DA analysis of gut bacteria. Relative abundances of (F) phylum, (G) class, (H) order, (I) family, and (J) genus in the relative abundance of various gut microbes among five groups. (a. WT group; b. Tg + vehicle group; c. Tg + HO group; d. Tg + Nano-HO group; e. Tg + Donepezil group). Data were shown as mean ± SEM (n = 6). $^{\#}$ $p < 0.05$ and $^{\#\#}$ $p < 0.01$ when compared with the WT group; * $p < 0.05$ and ** $p < 0.01$ when compared with the Tg + vehicle group; ▲ $p < 0.05$ and ▲▲ $p < 0.01$ when compared with the HO group. (K) A schematic drawing depicting the molecular mechanisms underlying the cognitive deficits ameliorating actions of Nano-HO in TgCRND8 mice.

TgCRND8 mice. Nano-HO treatment exerted better enhancement effect than HO on the relative abundance of *YS32* and *Bifidobacteriales* in TgCRND8 mice.

At the family level, totally 23 genera were identified (supplementary Fig. 2D). The proportion of *S24-7* was significantly decreased, but the proportions of *Ruminococcaceae*, *Lachbaccillace, Helicobacteraceae*, *Odoribacteraceae* and *Prevotellaceae* were markedly increased in TgCRND8 mice (Fig. 5I). Nano-HO treatment showed better inhibitory effect than HO on the proportions of *Helicobacteraceae* and *Odoribacteraceae* in TgCRND8 mice.

Finally, 22 genera were identified at the genus level (supplementary Fig. 2E). The relative abundance of *Akkermansia*, *Lactobacillus* and *Parabacteroides* was significant lower, while the proportions of *Allobaculum*, *Mucispirillum* and *Oscillospira* were higher in TgCRND8 mice (Fig. 5J). Nano-HO and HO had equal efficacy on reducing the relative abundance of *Akkermansia*, *Allobaculum*, *Lactobacillus*, *Oscillospira, Mucispirillum* and *Parabacteroides* in TgCRND8 mice.

Discussion

It is well-known that nano-particle is beneficial for prolonging exposure time, increasing drug efficacy and overcoming poor bioavailability. Droplet size of a nano-particle is the most critical factor since it is closely associated with the rate, extent and absorption of drug release. ZP is an electrokinetic potential at the slipping/shear plane of a colloid droplet moving under electric field in colloidal systems and nano-medicines. As an important indicator of stability, higher ZP of microemulsion indicates a higher stabilization to avoid degradation and aggregation [19]. In general, ZP values of microemulsions above ± 30 mV represent a relatively good stability. Low PDI reflects the uniformity of particle size and high ZP reflects the stability of nanoparticles [20]. In our study, Nano-HO formulation exhibited a relatively high negative ZP and a low PDI value, suggesting that it met the prerequisite for a stable microemulsion, which was consistent with the previous study [21]. In addition, small droplet size of Nano-HO may provide a large surface area for drug release into the aqueous phase. Our results showed that the accumulative release rate of HO from Nano-HO (86.3%) in PBS (pH 7.4) was significantly higher than that from regular HO (27.0%) over a period of 24 h (Fig. 1F).

Meanwhile, the pharmacokinetics results showed that C_{max} and AUC_{0-24} were higher in Nano-HO formulation, compared with the free HO, indicating improved absorption of HO from the GI tract. Compared with that of the free HO, $t_{1/2}$ was prolonged in the Nano-HO formulation, suggesting that Nano-HO circulate longer in the body. Additionally, relative bioavailability of Nano-HO was dramatically enhanced by 192.045% compared to free HO. It was rational to deduce that the increased solubility and improved release of Nano-HO collectively contribute to enhancement of bioavailability of Nano-HO, and better improvement on cognitive deficits in TgCRND8 mice. The better pharmacokinetic parameters observed in Nano-HO formulation might be due to the small droplet size that forms a large interfacial surface area for drug penetration into epithelial cells and enhanced absorption. Furthermore, a larger portion of formulas with long- and medium-chain fatty acids have the ability to by-pass portal circulation via lymphatic transport [22,23].

A large body of evidence has demonstrated that neuroinflammation is one of the major pathological factors of AD. Inflammation could induce BACE-1 expression, promote Aβ deposition, and exacerbate tau protein hyperphosphorylation and neuronal loss. Meanwhile, Aβ accumulation in AD causes microglia activation and astrocyte recruitment, thereby inducing the release of pro-inflammatory cytokines such as TNF-α, IL-6 and IL-1β [24]. Chemokines are a family of small molecules which play a role in development of neurodegenerative disorders due to their chemotactic activity on brain phagocytes. Activation of microglial is a central part of the chronic inflammatory process associated with amyloid plaques in AD. CCR2 was the first chemokine receptor shown to be associated with AD. In Tg2576 AD mice, CCR2 deficiency accelerates early disease progression by impairing the accumulation of mononuclear phagocytes [25]. APP-CCR2−/− mice exhibited higher Aβ levels and reduced CD11b + cell recruitment into the brain. Importantly, these mice showed higher mortality in a CCR2 gene dosage-dependent manner. Our results indicated that Nano-HO and free HO not only prevented the microgliosis, astrogliosis and Aβ deposits in the hippocampus and cortex (Fig. 3), and suppressed the release of TNF-α, IL-1β and IL-6, but also enhanced the production of CCR2 (Fig. 2F-I) in brains of TgCRND8 mice. Additionally, Nano-HO more effectively inhibited astrogliosis and improved CCR2 than HO in brain. These findings indicated that the amelioration of Nano-HO on hippocampal-dependent memory function may attribute to its anti-inflammatory property.

It is well-known that increased formation of Aβ plaques through sequential cleavage of APP by β- and γ-secretases also contribute to the pathogenesis of AD. Specifically, PS-1 and APH-1 are vital catalytic subsets of γ-secretase responsible for APP cleavage to Aβ. Meanwhile, proteolytic degradation is a particularly important determinant of cerebral Aβ levels, and Aβ-degrading enzymes including IDE and NEP play critical roles in Aβ degradation [26]. Our results demonstrated that both Nano-HO and HO inhibited the expressions of APH-1 and PS-1 (Fig. 4A). Interestingly, Nano-HO exerted better effects on inhibiting the expressions of p-APP (Thr 688) and BACE-1, and enhancing the expressions of NEP than HO. These results suggested that Nano-HO modulated APP processing through suppressing the activities of β- and γ-secretases and enhancing the activities of Aβ-degrading enzymes to clear Aβ deposition in TgCRND8 mice. Furthermore, our molecular docking results demonstrated that HO was well docked with BACE-1 at three active sites including Lys 107, Asp 216 and VAL 170 (supplementary Fig. 1), suggesting that HO may exert anti-AD effect as a BACE-1 inhibitor.

Another typical pathological hallmark of AD is abnormally aggregated tau hyperphosphorylation, which boosts reactive oxygen species (ROS) production, promotes inflammatory response, induces neuronal apoptosis, ultimately results in learning and memory impairments [27]. Notably, up-regulation of caspase-3 is directly responsible for cellular apoptosis in AD [28]. Our results revealed that Nano-HO inhibited tau hyperphosphorylation at Thr 205 and Ser 404 sites. Furthermore, Nano-HO down-regulated the expression of caspase-3, while it more effectively enhanced the expression of Bcl-2 in TgCRND8 mice than free HO (Fig. 4B). These observations indicated that the inhibitory effect of Nano-HO on specific site of tau hyperphosphorylation and apoptosis may be the molecular mechanisms underlying its cognitive function improving effects.

Activation of JNK pathway has been consistently found in the surrounding area of Aβ plaques via exaggerating p-Tau (Thr 205) [29]. Additionally, JNK pathway is also closely involved in the activation of GSK-3β, which is considered to be a key kinase responsible for APP phosphorylation in neuronal cells and aberrant tau phosphorylation [30]. GSK-3β could be inactivated by phosphorylation at Ser 9. Meanwhile, under pathological conditions, CDK5 was activated via direct binding to its neuronal specific activators p-35, subsequently aggravate tau hyperphosphorylation by enhancing GSK-3β, thereby exacerbating neuronal loss and neurodegeneration [31]. Therefore, agents that can up-regulate p-GSK-3β (Ser 9) or suppress CDK5 activity may ameliorate plaque pathology, neurofibrillary and neuronal loss in AD. In our present

study, Nano-HO markedly suppressed the ratio of p-JNK/JNK and p-35/CDK5, and more efficiently enhanced the ratio of p-GSK-3β (Ser9)/GSK-3β in TgCRND8 mice than free HO (Fig. 4D). These results suggested that the cognitive deficits improving effects of Nano-HO are associated with its ability to inhibit the activation of JNK/GSK-3β/CDK5 signaling pathway.

In recent years, aberrant gut microbiota has been implicated in AD pathogenesis and progression as it is associated with production of neurotransmitter-like products, formation of amyloid and causing inflammatory response. Neurotransmitters and neurotoxic substances produced by certain types of bacteria can enter the brain through systemic circulation to further affect nerve function, a phenomenon referred to "Microbiota-gut-brain axis" [32]. Previous study has demonstrated a strong association between cognitive dysfunction in SAMP8 mice and abnormal gut microbiota composition [33]. In our study, the α-diversity analysis results, including Shannon index and Simpson index, suggested a reduction in the diversity of the bacterial community in TgCRND8 mice (Fig. 5B-C), which was consistent with the similar decline of bacterial diversity in AD patients [34]. Then the structural variability or similarity among different groups was assessed by system clustering tree, PCA and PLS-DA (Fig. 5A, D, E). These results revealed that the bacteria community in the Nano-HO treatment group tended to recover to normal.

Specifically, fewer *Actinobacteria,* but more *Bacteroidetes* and *Proteobacteria* were found in the gut microbiota of AD patients and APP/PS1 transgenic mice [34]. Moreover, reduction in given beneficial bacteria such as *Firmicutes* spp. could increase inflammation. Metabolites secreted by *Firmicutes* spp. decreased the production of pro-inflammatory factors, leading to suppression of inflammation [35]. Intake of probiotics such as *Lactobacillales* spp. and *Bifidobacteriales* spp. could improve inflammatory condition and intestinal epithelial barrier function impairment [36]. Our results showed that in TgCRND8 mice, the proportions of *Actinobacteria* and *Firmicutes* decreased by 88% and 42.4% respectively, while *Proteobacteria*, *Bacteroidetes* and *Cyanobacteria* increased by 235.3%, 99.7% and 125%, respectively. Both of Nano-HO and HO treatments inhibited the relative abundance of the *Firmicutes*, *Proteobacteria*, *Bacteroidetes* and *Cyanobacteria* in TgCRND8 mice, and Nano-HO enhanced the relative abundance of *Actinobacteria* in a more potent manner than HO (Fig. 5F). Furthermore, declines in *Bifidobacteria* (at order level) and *Lactobacillus* (at genus level) by 87.3% and 69.7%, respectively, were observed in TgCRND8 mice (Fig. 5H and J), revealing that the reduction of beneficial bacteria was a potential cause of inflammation in TgCRND8 mice.

Moreover, mucin-degrading bacteria are identified as microbial drivers. Among them, *Prevotella* and *Ruminococcus* degrades mucin, while *Desulfovibrio* enhances the rate-limiting sulfatase step [37]. As probiotics strains, *Akkermansia* can secrete immunoglobulin A (IgA) and anti-bacterial peptides to exert anti-inflammatory and barrier-improving properties [38]. *Helicobacter pylori* filtrate could cause tau hyperphosphorylation in brains of rats via activation of GSK-3β [39]. Our results showed that the relative abundance of *Prevotellaceae* (at family level, Fig. 5I), *Ruminococcaceae* (at family level, Fig. 5I), *Desulfovibrionales* (at order level, Fig. 5H) and *Helicobacteraceae* (at family level, Fig. 5I) drastically increased to 325.6%, 139.3%, 457.6%, and 532.3%, respectively, in TgCRND8 mice. However, the proportion of *Akkermansia* (at genus level, Fig. 5J) was significantly decreased in TgCRND8 group. These changes may be of relevance to the increased transmembrane permeability. Nano-HO and HO reversed these changes in TgCRND8 mice, suggesting that Nano-HO and HO have protective effects on transmembrane permeability.

Fig. 5K schematically summarized the molecular mechanisms underlying the cognitive deficits ameliorating action of Nano-HO and HO in TgCRND8 mice.

Conclusions

Our study demonstrated for the first time that the protective effects of Nano-HO against cognitive deficits in TgCRND8 mice were mediated via inhibiting neuroinflammation and tau hyperphosphorylation, modulating APP processing through suppressing the activation of JNK/CDK5/GSK-3β signaling pathway. Furthermore, Nano-HO could also regulate the compositions of gut microbiota. Taken together, Nano-HO is a promising nano-based natural product worthy of further development into pharmaceutical treatment for AD.

Funding

This work was supported by Natural Science Foundation of Guangdong Province of China (project no. 2019A1515011257), the CUHK Direct Grant (project no. 2017.076) and Natural Science Foundation of China (project no. 81973519).

Authors' contribution

XYF and LZX conceived the research idea and designed the experimental protocols. QC performed the animal experiments and collected the experimental data. LQP analyzed the HPLC data. SZR provided and authenticated HO. ISP performed the data analysis. YQJ supervised the IHC staining. XQQ helped the animal experiments and checked the references. YW conducted the molecular docking. HYF prepared the Nano-HO formulation. QC drafted the manuscript. XYF and LZX revised the manuscript. All authors read and approved the final manuscript.

Compliance with Ethics Requirements

All Institutional and National Guidelines for the care and use of animals (fisheries) were followed.

Declaration of Competing Interest

The authors declare that they have no known competing financial interests or personal relationships that could have appeared to influence the work reported in this paper.

Appendix A. Supplementary material

Supplementary data to this article can be found online at https://doi.org/10.1016/j.jare.2021.03.012.

References

[1] Gee MS, Son SH, Jeon SH, et al. A selective p38α/β MAPK inhibitor alleviates neuropathology and cognitive impairment, and modulates microglia function in 5XFAD mouse. Alzheimers Res Ther 2020;12:45.
[2] Hamm V, Heraud C, Bott JB, et al. Differential contribution of APP metabolites to early cognitive deficits in a TgCRND8 mouse model of Alzheimer's disease. Sci Adv 2017;3:e1601068.
[3] Palop JJ, Mucke L. Amyloid-β-induced neuronal dysfunction in Alzheimer's disease: from synapses toward neural networks. Nat Neurosci 2010;12:812–8.
[4] Tiwari S, Atluri V, Kaushik A, et al. Alzheimer's disease: pathogenesis, diagnostics, and therapeutics. Int J Nanomed 2019;14:5541–54.
[5] Bossy-Wetzel E, Schwarzenbacher R, Lipton SA. Molecular pathways to neurodegeneration. Nat Med 2004;10:S2–9.
[6] Cui HS, Huang LS, Sok DE, et al. Protective action of honokiol, administered orally, against oxidative stress in brain of mice challenged with NMDA. Phytomedicine 2017;14:696–700.
[7] Zhang P, Liu XY, Zhu YJ, et al. Honokiol inhibits the inflammatory reaction during cerebral ischemia reperfusion by suppressing NF-kB activation and cytokine production of glial cells. Neurosci Lett 2013;534:123–7.
[8] Matsui N, Takahashi K, Takeichi M, et al. Magnolol and honokiol prevent learning and memory impairment and cholinergic deficit in SAMP8 mice. Brain Res 2009;1305:108–17.

[9] Xian YF, Ip SP, Mao QQ, et al. Honokiol improves learning and memory impairments induced by scopolamine in mice. Eur J Pharmacol 2015;760:88–95.
[10] Date AA, Desai N, Dixit R, et al. Self-nanoemulsifying drug delivery systems: formulation insights, applications and advances. Nanomedicine 2010;5:1595–616.
[11] Hyde LA, Kazdoba TM, Grilli. Age-progressing cognitive impairments and neuropathology in transgenic CRND8 mice. Behav Brain Res 2005;160:344–55.
[12] Chishti MA, Yang DS, Janus C. Early-onset amyloid deposition and cognitive deficits in transgenic mice expressing a double mutant form of amyloid precursor protein 695. J Biol Chem 2001;276:21562–70.
[13] Wang X, Wang YQ, Geng YL, et al. Isolation and purification of honokiol and magnolol from cortex Magnoliae officinalis by high-speed counter-current chromatography. J Chromatogr A 2004;1036:171–5.
[14] Xu ZZ, Yang J, Bai J, et al. Preparation and pharmacokinetic study of oral self-microemulsifying delivery systems containing honokiol. Chinese J New Drug 2012;21:857–62.
[15] Li HQ, Ip SP, Yuan QJ, et al. Isorhynchophylline ameliorates cognitive impairment via modulating amyloid pathology, tau hyperphosphorylation and neuroinflammation: Studies in a transgenic mouse model of Alzheimer's disease. Brain Behav Immune 2019;82:264–78.
[16] Wang DM, Dong XH, Wang CY. Honokiol ameliorates amyloidosis and neuroinflammation and improves cognitive impairment in Alzheimer's disease transgenic mice. J Pharmacol Exp Ther 2018;366:470–8.
[17] Zha L, Yu Z, Fang J, et al. NLRC3 Delays the Progression of AD in APP/PS1 Mice via Inhibiting PI3K Activation. Oxid Med Cell Longev 2020;4:1–14.
[18] Ramezani M, Komaki A, Hashemi-Firouzi N, et al. Therapeutic effects of melatonin-treated bone marrow mesenchymal stem cells (BMSC) in a rat model of Alzheimer's disease. J Chem Neuroanat 2020;108:101804.
[19] Honary S, Zahir F. Effect of zeta potential on the properties of nano-drug delivery systems - A review (Part 2). Trop J Pharm Res 2013;12:265–73.
[20] Guerra-Rosas MI, Morales-Castro J, Ochoa-Martínez LA, Salvia-Trujillo L, Martín-Belloso O. Long-term stability of food-grade nanoemulsions from high methoxyl pectin containing essential oils. Food Hydrocoll 2016;52:438–46.
[21] Dou YX, Zhou JT, Wang TT, et al. Self-nanoemulsfiying drug delivery system of bruceine D: a new approach for anti-ulcerative colitis. Int J Nanomedicine 2018;13:5887–907.
[22] Caliph SM, Charman WN, Porter CJ. Effect of short-, medium-, and long-chain fatty acid-based vehicles on the absolute oral bioavailability and intestinal lymphatic transport of halofantrine and assessment of mass balance in lymph-cannulated and non-cannulated rats. J Pharm Sci 2000;89:1073–84.
[23] Wu W, Wang Y, Que L. Enhanced bioavaiability of silymarin by self-microemulsifying drug delivery system. Eur J Pharm Biopharm 2006;63:288–94.
[24] Cai ZY, Hussain MD, Yan LJ. Microglia, neuroinflammation, and beta-amyloid protein in Alzheimer's disease. Int J Neurosci 2014;124:307–21.
[25] El Khoury J, Toft M, Hickman SE, et al. Ccr2 deficiency impairs microglial accumulation and accelerates progression of Alzheimer-like disease. Nat Med 2007;13:432–8.
[26] Chen GF, Xu TH, Yan Y, et al. Amyloid beta: structure, biology and structure-based therapeutic development. Acta Pharmacol Sin 2017;38:1205–35.
[27] Zhou H, Gong Y, Liu Y, et al. Intelligently thermoresponsive flower-like hollow nano-ruthenium system for sustained release of nerve growth factor to inhibit hyperphosphorylation of tau and neuronal damage for the treatment of Alzheimer's disease. Biomaterials 2020;237:119822.
[28] Louneva N, Cohen JW, Han LY, et al. Caspase-3 is enriched in postsynaptic densities and increased in Alzheimer's disease. Am J Pathol 2008;173:1488–95.
[29] Ploia A, Antoniou X, Sclip A. JNK plays a key role in tau hyperphosphorylation in Alzheimer's disease models. J Alzheimers Dis 2011;26:315–29.
[30] Phiel CJ, Wilson CA, Lee VM, et al. GSK-3α regulates production of Alzheimer's disease amyloid-β peptides. Nature 2003;423:435.
[31] Kimura T, Ishiguro K, Hisanaga S. Physiological and pathological phosphorylation of tau by Cdk5. Front Mol Neurosci 2014;7:65.
[32] Shen H, Guan Q, Zhang X, et al. New mechanism of neuroinflammation in Alzheimer's disease: The activation of NLRP3 inflammasome mediated by gut microbiota. Prog Neuropsychopharmacol Biol Psychiatry 2020;100:109884.
[33] Zhan G, Yang N, Li S, et al. Abnormal gut microbiota composition contributes to cognitive dysfunction in SAMP8 mice. Aging 2018;10:1257–67.
[34] Vogt NM, Kerby RL, Dill-McFarland KA, et al. Gut microbiome alterations in Alzheimer's disease. Sci Rep 2017;7:13537.
[35] Orbe-Orihuela YC, Lagunas-Martínez A, Bahena-Román M, et al. High relative abundance of firmicutes and increased TNF-α levels correlate with obesity in children. Salud Publica Mex 2017;60:5–11.
[36] Laparra JM, Sanz Y. Bifidobacteria inhibit the inflammatory response induced by gliadins in intestinal epithelial cells via modifications of toxic peptide generation during digestion. J Cell Biochem 2010;109:801–7.
[37] Ijssennagger N, Belzer C, Hooiveld GJ, et al. Gut microbiota facilitates dietary heme-induced epithelial hyperproliferation by opening the mucus barrier in colon. Proc Natl Acad Sci USA 2015;112:10038–43.
[38] Hidalgo-Cantabrana C, Delgado S, Ruiz L, et al. Bifidobacteria and their health-promoting effects. Microbiol Spectr 2017;5(3).
[39] Wang XL, Zeng J, Yang Y, et al. Helicobacter pylori filtrate induces Alzheimer-like tau hyperphosphorylation by activating glycogen synthase kinase-3β. J Alzheimers dis 2015;43:153–65.